JNeurosci
THE JOURNAL OF NEUROSCIENCE

Research Articles: Cellular/Molecular

Strengthening of the efferent olivocochlear system leads to synaptic dysfunction and tonotopy disruption of a central auditory nucleus

Mariano N. Di Guilmi[1], Luis E. Boero[1,2], Valeria C. Castagna[2], Adrián Rodríguez-Contreras[3], Carolina Wedemeyer[1], María Eugenia Gómez-Casati[2] and Ana Belén Elgoyhen[1,2]

[1]*Instituto de Investigaciones en Ingeniería Genética y Biología Molecular, Dr. Héctor N Torres, INGEBI-CONICET, Buenos Aires, Argentina. (C1428ADN)*

[2]*Instituto de Farmacología, Facultad de Medicina, UBA, Buenos Aires, Argentina. (C1121ABG)*

[3]*Department of Biology, the City College of the City University of New York, New York, NY, USA. (NY 10031)*

https://doi.org/10.1523/JNEUROSCI.2536-18.2019

Received: 2 October 2018

Revised: 10 June 2019

Accepted: 14 June 2019

Published: 19 June 2019

Author contributions: M.N.D.G., M.E.G.-C., and A.B.E. designed research; M.N.D.G., L.E.B., V.C.C., A.R.-C., C.W., and M.E.G.-C. performed research; M.N.D.G., L.E.B., V.C.C., C.W., and M.E.G.-C. analyzed data; M.N.D.G. wrote the first draft of the paper; M.N.D.G., L.E.B., A.R.-C., C.W., M.E.G.-C., and A.B.E. edited the paper; M.N.D.G. wrote the paper; A.R.-C., M.E.G.-C., and A.B.E. contributed unpublished reagents/analytic tools.

Conflict of Interest: The authors declare no competing financial interests.

We thank Eleonora Katz, Lucas G. Vattino and Marcelo J. Moglie for critical reading of the manuscript, Juan D. Goutman for fruitful discussion and assistance with data analysis through routines implemented in Igor Pro. We also thank Claudia Gatto for excellent technical assistance. This work was supported by Agencia Nacional de Promoción Científica y Tecnológica (ABE and MNDG), Argentina and Scientific Grand Prize from the Fondation Pour l´Audition (A.B.E.), NIH Grant R01 DC001508 (Paul A. Fuchs and A.B.E.) and SC1DC015907 (AR-C). MNDG is the recipient of The Company of Biologist travelling fellowship (DEVTF-160703) and a “Bec.Ar” fellowship for a short stay supported by the Argentinian government.

Address for Correspondence: Ana Belén Elgoyhen, Instituto de Investigaciones en Ingeniería Genética y Biología Molecular “Dr. Héctor Torres” (INGEBI-CONICET). Buenos Aires. Argentina, Vuelta de Obligado 2490, (C1428ADN) Buenos Aires, Argentina, e-mail: elgoyhen@dna.uba.ar, abelgoyhen@gmail.com, TE: +541147832871, FAX: +54117868578

Cite as: J. Neurosci 2019; 10.1523/JNEUROSCI.2536-18.2019

Journal section: Cellular & Molecular

Strengthening of the efferent olivocochlear system leads to synaptic dysfunction and tonotopy disruption of a central auditory nucleus

Abbreviated title: MNTB tonotopy is disrupted in *Chrna9 L9'T* mice

Authors

Mariano N. Di Guilmi[1]*, Luis E. Boero[1,2], Valeria C. Castagna[2], Adrián Rodríguez-Contreras[3], Carolina Wedemeyer[1], María Eugenia Gómez-Casati[2] and Ana Belén Elgoyhen[1,2*].

[1] Instituto de Investigaciones en Ingeniería Genética y Biología Molecular, Dr. Héctor N Torres, INGEBI-CONICET, Buenos Aires, Argentina. (C1428ADN)

[2] Instituto de Farmacología, Facultad de Medicina, UBA, Buenos Aires, Argentina. (C1121ABG)

[3] Department of Biology, the City College of the City University of New York, New York, NY, USA. (NY 10031)

* To whom correspondence should be addressed

Address for Correspondence:

Ana Belén Elgoyhen

Instituto de Investigaciones en Ingeniería Genética y Biología Molecular "Dr. Héctor Torres" (INGEBI-CONICET). Buenos Aires. Argentina

Vuelta de Obligado 2490, (C1428ADN) Buenos Aires, Argentina

e-mail: elgoyhen@dna.uba.ar, abelgoyhen@gmail.com

TE: +541147832871

FAX: +54117868578

Mariano Nicolás Di Guilmi

Instituto de Investigaciones en Ingeniería Genética y Biología Molecular “Dr. Héctor Torres” (INGEBI-CONICET). Buenos Aires. Argentina

Vuelta de Obligado 2490, (C1428ADN) Buenos Aires, Argentina

e-mail: mndiguilmi@dna.uba.ar; mndiguilmi@gmail.com

TE: +541147832871

FAX: +54117868578

Number of pages: 38

Number of figures: 7

Number of tables: 3

Number of multimedia: 0

Number of 3D models: 0

Number of words in abstract: 232

Number of words in Introduction: 633

Number of words in Discussion: 1500

Conflict of Interest: The authors declare no conflict of interests.

Acknowledgements. We thank Eleonora Katz, Lucas G. Vattino and Marcelo J. Moglie for critical reading of the manuscript, Juan D. Goutman for fruitful discussion and assistance with data analysis through routines implemented in Igor Pro. We also thank Claudia Gatto for excellent technical assistance. This work was supported by Agencia Nacional de Promoción Científica y Tecnológica (ABE and MNDG), Argentina and Scientific Grand Prize from the Fondation Pour l´Audition (A.B.E.), NIH Grant R01 DC001508 (Paul A. Fuchs and A.B.E.) and SC1DC015907 (AR-C). MNDG is the recipient of The Company of Biologist travelling fellowship (DEVTF-160703) and a "Bec.Ar" fellowship for a short stay supported by the Argentinian government.

Keywords: α9α10 nAChR, *Chrna9L9'T*, efferent MOC inhibition, tonotopy, MNTB

Abstract

The auditory system in many mammals is immature at birth but precisely organized in adults. Spontaneous activity in the inner ear plays a critical role in guiding this maturation process. This is shaped by an efferent pathway that descends from the brainstem and makes transient direct synaptic contacts with inner hair cells (IHCs). In this work, we used an α9 cholinergic nicotinic receptor knock-in mouse model (of either sex) with enhanced medial efferent activity (*Chrna9L9'T*, *L9'T*) to further understand the role of the olivocochlear system in the correct establishment of auditory circuits. Wave III of auditory brainstem responses (which represents synchronized activity of synapses within the superior olivary complex) was smaller in *L9'T* mice, suggesting a central dysfunction. The mechanism underlying this functional alteration was analyzed in brain slices containing the medial nucleus of the trapezoid body (MNTB), where neurons are topographically organized along a medio-lateral axis. The topographic organization of MNTB physiological properties observed in WT was abolished in *L9'T* mice. Additionally, electrophysiological recordings in slices indicated MNTB synaptic alterations. *In vivo* multielectrode recordings showed that the overall level of MNTB activity was reduced in the *L9'T*. The present results indicate that the transient cochlear efferent innervation to IHCs during the critical period before the onset of hearing is involved in the refinement of topographic maps as well as in setting the properties of synaptic transmission at a central auditory nucleus.

Significance Statement

Cochlear inner hair cells of altricial mammals display spontaneous electrical activity before hearing onset. The pattern and firing rate of these cells are crucial for the correct maturation of the central auditory pathway. A descending efferent innervation from the central nervous system contacts the hair cells during this developmental window. The present work shows that genetic enhancement of efferent function disrupts the orderly topographic distribution of biophysical and synaptic properties in the auditory brainstem and causes severe synaptic dysfunction. This work adds to the notion that the transient efferent innervation to the cochlea is necessary for the correct establishment of the central auditory circuitry.

Introduction

The strength and physiological properties of synaptic inputs, the accurate organization of neuronal circuits and the formation of topographic maps in the mature brain are established during development through activity-dependent processes that involve reorganization and fine tuning of immature synaptic and cellular networks (Goodman and Shatz, 1993; Hanson and Landmesser, 2004; Kirkby et al., 2013). The auditory system in many mammals is very immature at birth but precisely organized in adults. Spontaneous activity in the inner ear during an early developmental critical period comes into play to guide this process (Lippe, 1994; Kotak and Sanes, 1995; Jones et al., 2007; Tritsch et al., 2007; Sonntag et al., 2009). Spontaneous activity, driven by calcium action potentials in the IHCs (Kros et al., 1998; Glowatzki and Fuchs, 2000; Marcotti et al., 2003; Tritsch et al., 2007; Johnson et al., 2011), is essential for several processes related to the survival of target neurons in the cochlear nucleus (Leake et al., 2006), the accurate wiring of auditory pathways (Friauf and Lohmann, 1999) and the refinement of tonotopic maps in the lateral superior olive (Kandler, 2004; Clause et al., 2014).

A distinctive feature of IHCs during the prehearing critical period is the presence of direct axo-somatic efferent medial olivocochlear (MOC) synaptic contacts, which disappear at hearing onset (Warr and Guinan, 1979; Simmons et al., 1996). This synapse is cholinergic (Glowatzki and Fuchs 2000; Katz et al., 2004, Gomez-Casati et al., 2005) and is mediated by a highly calcium permeable α9α10 nicotinic cholinergic receptor (nAChR) present in the IHCs (Elgoyhen 1994, 2001; Weisstaub et al., 2002; Lipovsek et al., 2012) coupled to the activation of small conductance calcium-activated SK2 potassium channels (Glowatzki and Fuchs, 2000). Exogenously applied acetylcholine (Glowatzki and Fuchs, 2000) or electrical stimulation of the efferent terminals (Goutman et al., 2005; Wedemeyer et al., 2018) inhibit IHC action potentials. Therefore, it has been proposed that cholinergic efferent inhibition of IHCs might

impose rhythmicity to the generation of IHC action potentials and the spontaneous activity of the auditory pathway during the critical period preceding hearing onset (Glowatzki and Fuchs, 2000; Johnson et al., 2011; Sendin et al, 2014; Moglie et al., 2018). However, this notion has been challenged (Tritsch et al., 2010a) and therefore the function of the developmental efferent innervation is still a matter of debate.

Clause et al. (2014) showed that in α9 knock-out mice, which lack efferent activity (Vetter et al., 1999; 2007), the spike patterning of spontaneous activity at the MNTB level is altered. This leads to a reduced permanent sharpening of functional topography (Clause et al., 2014) and to the impairment of sound localization and frequency processing (Clause et al., 2017), indicating a role of the efferent system in the development of central auditory nuclei. The present work shows an alternative approach in which we used an α9 knock-in mouse model (*L9´T*) with enhanced efferent activity (Taranda et al., 2009) leading to sustained inhibition of IHC action potential generation (Wedemeyer et al., 2018). Since a decrease of efferent modulation leads to an alteration in the functional topography (Clause et al., 2014), one could *a priori* hypothesize that the enhancement of efferent strength might lead to hyper refinement of topographic properties. To this end, we analyzed the calyx of Held - MNTB synapse, making focus on MNTB innervation, its synaptic features and topography. Synaptic transmission was greatly impaired in α9 *L9´T* mice. Moreover, the proportion of immature “small”-evoked postsynaptic currents (EPSCs) was significantly enhanced in *L9´T* mice. Contrary to our hypothesis, a complete lack of topographic organization of the MNTB was observed. These results taken together with those of Clause et al. (2014) provide clear evidence that a tight regulation of pre-hearing spontaneous activity, brought about by the transient MOC innervation to the IHCs, is crucial for the development of the central auditory pathway.

Methods

Animals and experiments. Generation of the knock-in mouse (*L9'T*) has been described previously (Taranda et al., 2009). Wild-type (WT) or homozygous *L9'T* mice of either sex were used. All experimental protocols were carried out in accordance with the American Veterinary Medical Associations' AVMA Guidelines on Euthanasia (2013) and approved by the IACUC at INGEBI and CCNY.

Auditory brainstem responses (ABRs). Animals of postnatal days (P) 14, 16 and 21 were anesthetized with a mix of xylazine (10 mg/kg i.p.) / ketamine (100 mg/kg i.p) and needle electrodes were inserted at vertex and pinna, with a ground near the tail. ABRs were evoked with 5 ms tone pips (0.5 ms rise-fall, cos2 onset, at 35/s). The response was amplified (10000X) filtered (0.1-3 kHz) and averaged with an A-D board in a LabVIEW-driven data-acquisition system (National Instruments, Austin, Texas, USA, RRID:SCR_014325). Sound level was raised in 5 dB steps from 20 dB to 80 dB SPL. At each level, 1024 responses were averaged (with stimulus polarity alternated), using an "artefact reject" whereby response waveforms were discarded when peak-to-peak amplitude exceeded 15 μV. Upon visual inspection of stacked waveforms, "threshold" was defined as the lowest SPL level at which a wave could be detected. ABR wave I amplitude was measured baseline to positive first peak and waves II to V were measured peak to peak, computed by off-line analysis of stored waveforms using Clampfit 10.3 (Molecular Devices, LLC, San José, CA, USA).

Electrophysiology on MNTB slices. For slice recordings, 50 mice of either sex between 12 and 14 postnatal days old were used. Their brains were removed rapidly after decapitation and placed into an ice-cold low-Ca^{2+} artificial cerebrospinal fluid solution (aCSF). This solution contained the following (in mM): 125 NaCl, 2.5 KCl, 3 $MgCl_2$, 0.1 $CaCl_2$, 1.25 NaH_2PO_4, 0.4 ascorbic acid, 3 myoinositol, 2 pyruvic acid, 25 D-glucose, and 25 $NaHCO_3$. The brainstem was glued on a cooled chamber of a vibrating microslicer (Vibratome 1000 Plus, Ted Pella, California, USA). Transverse slices (300

μm thickness) containing the MNTB were sequentially cut and transferred into an incubation chamber containing normal aCSF at 37°C for 30 min. After incubation, slices were allowed to return to room temperature. Normal aCSF had the same composition as the slicing solution except that the $MgCl_2$ and $CaCl_2$ concentrations were 1 and 2 mM, respectively. The pH was 7.4 when gassed with 95% O_2 and 5% CO_2.

Whole-cell patch-clamp recordings. Slices were transferred to an experimental chamber. During recording, slices were continuously perfused with carbogenated (95% O_2 and 5% CO_2) aCSF maintained at room temperature (22–25°C). Medial (M) and lateral (L) MNTB principal cells were compared in order to evaluate topographic differences. The position of these two opposite groups of cells was determined during the experiment according to the morphological landmark delimited by the middle line (M) and the VII cranial nerve (L). Lucifer Yellow (0.3 mg/ml; Sigma Aldrich) was added to the internal solution to certify the position at the end of the experiment. MNTB neurons were visualized using a Zeiss Axioskop microscope (Oberkochen, Germany) and viewed with differential interference contrast by a 40X water-immersion objective (0.8 numerical aperture water-immersion objective) and a camera with contrast enhancement (DMK 23UP1300, The Imaging Source, North Carolina, USA). Whole-cell recordings were made with patch pipettes pulled from thin-walled borosilicate glass (World Precision Instruments, Florida, USA, RRID:SCR_008593). Electrodes had resistances of 3.8 to 4.5 MΩ. Potassium currents were isolated by an internal solution containing (mM): k-gluconate 121.3, KCl 20, Hepes 10, phosphocreatine 10, EGTA 0.5, Mg-ATP 4, Li-GTP 0.3. Additionally, the external solution was supplemented with TTX (1 μm), $CdCl_2$ (50 μm) and ZD7288 (10 μm). Hyperpolarization-activated currents (I_h-type) were analyzed from recordings in the presence of TTX (1 μM) and TEA (20 mM). The pH was adjusted to 7.3 with KOH. The pipette solution used for isolating synaptic currents was (in mM): Cs-$MeSO_3$ 135, TEA-Cl 13, HEPES 5, $MgCl_2$ 3.5, $CaCl_2$ 0.1,

198 Na_2-ATP 2.5, EGTA 1; pH 7.2 (CsOH). Liquid junction potential was uncompensated in
199 both solutions.

200 Patch clamp recordings were made using an Axopatch 200A (Molecular Devices, San
201 Jose, CA, USA) amplifier, a Digidata 1320 (Molecular Devices, San Jose, CA, USA)
202 and pClamp 9.0 software (Molecular Devices, San Jose, CA, USA;
203 RRID:SCR_011323). Data were sampled at 50 kHz and filtered at 4-6 kHz (low pass
204 Bessel). Series resistances ranged from 6 to 15 MΩ. Whole-cell membrane
205 capacitance (15-25 pF) was registered from the amplifier after compensation of the
206 transient generated by a 10 ms voltage step. To elicit action potentials, positive current
207 steps (250 pA) during 500 ms were applied. Thus, the delay in action potential
208 generation for the same current step was compared in medial and lateral cells.
209 Voltage-clamp protocols were as follows: the cell was held at a resting potential of −50
210 mV (1 sec) and stepped to a range of −130 mV to -40 mV for 500 ms (in increments of
211 5 mV). I_h amplitude was measured as instantaneous (I_I) minus slowly inward (I_s) current
212 (I_S − I_I; Yi et al., 2010). Statistical comparisons were evaluated at its maximal current
213 amplitude (-140 mV). ZD7288 (50 μM) or CsCl (1 mM) were used to confirm the
214 presence of an I_h current. No leak current was subtracted from any of the raw current
215 traces for the I_h current. Potassium currents were elicited by square depolarizing pulses
216 of 1s from -90 to +40 mV. Off-line leak subtraction was performed for K^+ currents and
217 the average current at the steady-state (within the last 50 ms) is reported.

218 Miniature excitatory post synaptic currents (mEPSCs) were recorded continuously for
219 at least three separate periods of 1 min. Amplitude and frequency were analyzed using
220 Clampfit 10.3 (Molecular Devices, San Jose, CA, USA) and Mini Analysis Program
221 (Synaptosoft, Decatur, GA, RRID:SCR_002184). Events with a maximal duration of 5
222 ms and decay time less than 1.5 ms were considered (Taschenberger et al., 2005;
223 Rusu and Borts, 2010). EPSCs were evoked by stimulating the globular bushy cell
224 axons in the trapezoid body at the midline using a hand-made bipolar platinum

electrode and an isolated stimulator (Digitimer DS3; Hertfordshire, UK) (0.1 ms duration and 2–20 mA amplitude). Strychnine (1 μM) was added to the aCSF to block inhibitory glycinergic synaptic responses. Classification of "small" and "large" EPSC was made according to the literature. Typically, a canonical mature MNTB EPSC amplitude ("large") is in the 5 to 15 nA range (Barnes-Davies et al., 1995, Borst et al., 1995, Erazo Fisher et al., 2007, Xiao et al., 2013). In the present work, it was bigger than 4 nA in WT animals. On the contrary, poly-innervated MNTB cells display "small" EPSC amplitudes in the pico-amperes range (Rodríguez-Contreras et al., 2008) and they were smaller than 1 nA in the present work. Additionally, both types of current amplitudes display different stimulus-intensity behaviour. "Large" (mono-innervated) EPSCs are independent from stimulus intensity whereas "small" (multi-innervated) EPSCs are dependent on stimulus intensity (see Fig. 5) due to the increased number of fibers which are recruited as the stimulus is raised. Data distribution was evaluated by fitting with a gaussian function (extreme value distribution) with the Statistica Software (Stat Soft. Inc, Tulsa, Ok, RRID:SCR_014213). This distribution allows to evidence the largest extreme.

Analysis of electrophysiological data. Electrophysiological recordings were analyzed using Clampfit 10.3 (Molecular Devices, San Jose, CA, USA) and custom routines in Igor 6.2 (Wavemetrics, Portland, OR, USA, RRID:SCR_000325). Igor routines were used to perform offline leak subtraction (for potassium currents). Series resistances of EPSC recordings was ~ 50-70% compensated. The remaining Rs error of postsynaptic currents was corrected by an off-line Igor routine.

***In vivo* electrophysiological recordings**. The surgical procedures used are those described by Rodríguez-Contreras et al. (2008), with some minor modifications. Neonate (P7-8) mice pups were initially anesthetized with isoflurane (3%, carried by oxygen). Animals were tracheotomized, intubated, and mechanically ventilated using a MiniVent type 845 (Harvard Apparatus, South Natick, MA, USA) mouse ventilator (190

breaths per minute, 30-40 µl stroke volume). During surgery, anesthesia was reduced to 1.5% and carefully monitored on the basis of pedal reflexes. A small craniotomy (1.5x1.5 mm) was performed and the vascular landscape constituted by the basilar artery and the anterior inferior cerebellar artery was exposed. The dura was carefully removed. A silicon probe (polytrode 4x4 16-channel arrays, NeuroNexus, A4x4-3mm-50-125-177-A16; ~1 MΩ) was coated with the lipophylic dye DiI (Molecular Probes, Eugene, OR, USA) for histological analysis after recording to confirm proper targeting to the MNTB. Recordings were acquired for 10 minutes and isoflurane was kept at 0.5%. All data from the silicon probe were sampled (20 kHz), amplified and digitized in a single head-stage (Intan RHD200-RHD2216, Intan Technologies LLC, Los Angeles, CA, USA). The signal obtained from the electrode was low-pass filtered (Butterworth, 4 poles, cut-off frequency 300 Hz) and processed by Offline Sorter 4.4 (Plexon; Dallas, Texas, USA). Spikes with amplitudes larger than 0.5% of the threshold noise were considered. Multi-unit activity collected in different active channels in every polytrode was averaged.

Experimental Design and Statistical Analysis. Experiments were designed in order to reduce the number of animals but taking into account a balance between the number of samples to accurately perform statistical tests and the ethics guidelines for animal research as described above. Data analyses were done blind to genotype. All statistical tests were carried out with Statistica 7.0 software (Stat Soft. Inc, Tulsa, OK, USA, RRID:SCR_014213) with the exception of ABRs performed with Prism 6 software (GraphPad, La Jolla, CA, USA, RRID: 294 SCR_002798). Prior to performing any analysis, data sets were tested for normal distribution and homoscedasticity. If these assumptions were satisfactorily passed, a parametric test was applied. In these cases, comparisons were made by one-way ANOVA and the statistic “F” value with the associated “p-value” significance was reported in every case. Otherwise, non-parametric Mann-Whitney test was used. Values of $p<0.05$ were considered significant.

279 Average data were expressed and plot as mean ± S.E.M. In all cases “n” indicates the
280 number of cells tested, with the exception of ABRs and *in vivo* recordings where “n” are
281 the number of animals.

282 **Drugs and reagents**. All drugs and reagents were purchased from Sigma-Aldrich
283 (Saint Louis, Missouri, USA, RRID:SCR_008988) with the exception of ZD7288 and
284 TTX which were purchased from Tocris Bioscience (Bristol, UK; RRID: SCR_003689).

Results

The overall MNTB activity is reduced in *L9'T* mice

The MOC-IHC synapse of *L9'T* mice displays both pre- and postsynaptic alterations leading to an enhancement and prolongation of inhibitory synaptic responses (Wedemeyer et al., 2018). Furthermore, low-frequency stimulation of MOC fibers allows a complete suppression of IHC action potentials in mutant mice (Wedemeyer et al., 2018). Developmental spontaneous activity generated in the cochlea is transmitted along the entire auditory pathway (Tritsch et al., 2010a). In order to analyze if MNTB spontaneous activity is altered in *L9'T* mice, we recorded *in vivo* the multiunit activity at P7-P8 in an ensemble of MNTB cells using polytrodes (silicon multielectrode probes) in both genotypes (Fig. 1A). In WT mice the mean MNTB firing rate (11.49±3.58 Hz, n=6 animals) was larger than in *L9'T* (2.53±0.43, n=8 animals; Mann-Whitney U Test, $Z=2.19$, $p=0.028$). This indicates that the overall level of MNTB spiking activity is reduced in the *L9'T* efferent gain of function mouse model compared to WT mice (Fig. 1B).

Reduction of ABR wave III amplitude in *L9'T* mice.

In order to examine whether this enhanced MOC efferent cholinergic strength and reduced overall MNTB spontaneous activity has an impact on the functionality of the auditory pathway, auditory brainstem responses (ABRs) were measured at P16 (temporally close to the onset of hearing) and at P21 (considered as an auditory mature stage: Fig. 2, Table 1 and Table 2). ABR individual waves reflect the activation of subsequent auditory processing stations and were used as a functional hearing test that detects retro-cochlear abnormalities underlying hearing impairment (Karplus et al., 1988; Shapiro, 1988; Shaw, 1988). Pip-evoked ABR waveform amplitudes were analyzed at 80 dB SPL for peaks corresponding to the auditory nerve (wave I), cochlear nucleus (wave II) and superior olivary complex (SOC) (wave III) at different

311 frequencies (8, 16 and 32 KHz) (Melcher et al., 1996; Kim et al., 2013) (Fig. 2A).
312 Interestingly, peak III amplitude at P16 was reduced in *L9'T* mice compared to WT at 8
313 KHz and at all frequencies tested at P21 (Table 1 and Fig 2D). Given the wide variation
314 between the amplitudes of wave I among animals, we normalized wave III amplitudes
315 to those of wave I. Significant differences in amplitude ratios between WT and *L9'T*
316 mice were still observed at 16 and 32 KHz at P21 (Table 1), indicating a central
317 functional abnormality at the level of the SOC. Latencies were similar for both
318 genotypes (Table 2), suggesting no alterations in the speed of transmission. These
319 results show that a cochlear enhancement of α9α10 nAChR activity results in a central
320 dysfunction at the brainstem level. Moreover, wave II amplitudes were also reduced in
321 *L9'T* mice at P16, but similar at P21 when compared to WT (Table 1 and Fig. 2C).
322 These might indicate differential effects in the maturation of different nuclei of the
323 auditory pathway in mutant mice. As recently shown (Boero et al., 2018), no
324 abnormalities in peak I amplitude were observed in *L9'T* compared to WT mice at 8, 16
325 and 32 KHz, either at P16 or P21 (Fig. 2B; Table 1). This suggests no gross alterations
326 in the first synapse of the auditory pathway between IHCs and auditory nerve fibers in
327 *L9'T* mice. It should be noted that although no overall wave I changes were observed in
328 mutant mice, cochlear alterations have been reported in *L9'T* since they have fewer
329 ribbon synapses at the medial region and elevated auditory thresholds (Boero et al.,
330 2018, Taranda et al., 2009).

331

332 **Impairment of synaptic transmission at the calyx of Held in *L9'T* mice**

333 The reduction of ABR peak III amplitude in *L9'T* mice temporally close to the onset of
334 hearing, raises the question of whether synaptic transmission at the MNTB level is
335 altered in mice with enhanced MOC activity. To address this point, we performed
336 synaptic studies on slices containing the glutamatergic MNTB-calyx of Held synapse.
337 The rate and amplitude of mEPSCs (Fig. 3A) were recorded in the presence of TTX (1

338 μM). No differences were observed in mEPSCs amplitude distributions in *L'9T*
339 compared to WT (Fig. 3B.i), even when comparing the mean amplitudes along the
340 medio-lateral axis (WT M: 32.81±2.61 pA, n=8, 7 animals; WT L: 28.37±2.79 pA, n=12,
341 8 animals; ANOVA, F:1.21, p=0.285; *L'9T* M: 32.82±2.77 pA, n=18, 14 animals; *L'9T* L:
342 34.28±1.55 pA, n=16, 13 animals; Mann-Whitney test, Z:-0.66; p=0.512, Fig. 3B.ii).
343 However, mEPSC frequency displayed a larger dispersion in *L'9T* mice (Fig. 3C.i), due
344 to an increased mean mEPSC frequency in the lateral region (M: 2.52±0.56 Hz; L:
345 7.17±1.94 Hz; Mann-Whitney test, Z: -2.11, p=0.035), that was not observed in WT
346 mice (M: 2.07±0.51 Hz; L: 2.34±0.42 Hz, ANOVA, F:1.16, p=0.689; Fig. 3C.ii). This
347 result suggests that spontaneous transmitter release at the calyx of Held – MNTB
348 synapse is altered in *L9'T* mice.

349 Principal neurons of the MNTB receive synaptic input from a single giant calyx terminal
350 that generates the stereotyped calyceal EPSC response, which is independent of
351 stimulus intensity above threshold (Fig.4A and 4E). A broader EPSC amplitude
352 distribution in *L9'T* compared to WT mice was observed at P12-14 (Fig. 4B). Thus,
353 while no significant differences in the unitary medial and lateral EPSC amplitudes were
354 recorded in WT mice (M: 7.59±1.12 nA, n=9, 7 animals; L: 7.35±0.95 nA, n=10, 8
355 animals, ANOVA, F:0.027, p=0.87), the evoked synaptic currents in the lateral side
356 (5.07±0.87 nA, n=12, 11 animals) of *L9'T* mice were smaller compared to those of the
357 medial side (8.05±1.37 nA, n=11, 11 animals; ANOVA, F:5.07, p=0.0357, Fig.4D).
358 Interestingly, a broader dispersion of EPSC amplitudes in *L9'T* (Cv: 0.681) compared to
359 WT (Cv: 0.241) mice was still observed in P20-24 mice (Fig. 4F). However, no
360 significant differences in EPSC mean amplitudes in *L9'T* compared to WT were
361 evidenced at P20-24. Taken together, these results suggest that both spontaneous and
362 evoked synaptic transmission were impaired in *L9'T* mice, with the lateral low
363 frequency region being the most affected.

364

Immature synaptic responses in *L9'T* principal cells

During early development, presynaptic calyx of Held terminals make multiple small contacts on MNTB neurons. This is followed by an early stage of functional and structural transformation (Kandler and Friauf, 1993; Taschenberger et al., 2002; Wimmer et al., 2006; Rodriguez-Contreras et al., 2008) in which multiple inputs strengthen and compete until a final single innervation is established (Holcomb et al., 2013). These multiple early contacts elicit "small"-amplitude glutamatergic currents from each axon (Rodriguez-Contreras et al., 2008; Fig. 5A, left) until a mature calyceal response is established displaying a large, stimulus-independent response (Fig. 5A, right). Thus, the proportion of "small" *versus* "large" responses are reduced with maturation (Rodriguez-Contreras et al., 2008). Given that both "large" and "small" excitatory inputs to MNTB can be distinguished by their electrophysiological profile, the prevalence of small currents in both genotypes was analyzed (Fig. 5B). The probability of finding "small" inputs in WT mice was 10% (4 of 35 cells, 11 animals) at P12-P14, whereas this proportion was three-fold larger in *L9'T* mice reaching 31% (12 of 38 cells, 12 animals; Chi-squared test, χ^2=4.32, df=1, p=0.019).

Altered topographic organization of MNTB action potential waveforms in *L9'T* mice.

Figures 1 – 5 present evidence for both synaptic and connectivity impairments between calyx of Held terminals and MNTB principal cells in *L9'T* mice. In order to analyze if these alterations were also accompanied by the disruption of the MNTB topographic arrangement, the medio-lateral gradient of different biophysical neuronal properties was analyzed (Fig. 6A).

In the first place we analyzed the neuronal resting properties. In WT mice, the resting membrane potential (RMP) was more depolarized for medial (-54.27±0.47 mV, n=7; 5

391 animals) than lateral cells (-59.49±0.36 mV, n=6, 5 animals; ANOVA, F:9.33, p=0.0013)
392 (Fig. 6B). However, this difference was absent in the *L9'T* mouse model (M: -
393 59.57±0.53 mV, n=8, 7 animals; L: -58.57±0.79 mV, n=7, 7 animals; ANOVA, F:0.136,
394 p=0.72).

395 Like other neurons, MNTB principal cells can elicit an action potential (AP) after a
396 positive current injection (Fig. 6A) displaying waveform changes along the tonotopic
397 map (Leao et al., 2006). MNTB cells in WT presented a topographic distribution in AP
398 amplitudes (L>M, 8.6%; Fig. 6C), after-hyperpolarization (AHP; M>L, 27.9%; Fig. 6D),
399 area (L>M, 42.9%; Fig. 6E) and delay (L>M, 47.67%; Fig. 6F). However, none of these
400 parameters showed medio-lateral differences in *L9'T* mice (Fig. 6C-F and Table 3).
401 These results demonstrate that, contrary to WT mice, at the MNTB level neither the
402 RMP nor the AP waveform of MNTB principal cells show a medio-lateral differential
403 distribution in mice with enhanced MOC activity.

404

405 **Lack of medio-lateral gradient of potassium current amplitudes in *L9'T* mice**

406 Hyperpolarization-activated cyclic nucleotide-gated (HCN) channels, permeable to both
407 Na^+ and K^+, are responsible for the inward I_h rectifying current which is present in many
408 auditory neurons and can influence neuronal excitability (Bal and Oertel, 2000). The
409 combination of I_h and potassium currents allow the accurate relay of high frequency
410 auditory information across MNTB neurons and thus the fidelity by which timing
411 information is computed (Hooper et al., 2002; Barnes-Davies et al., 2004; Hassfurth et
412 al., 2009; Mathews et al., 2010; Karcz et al., 2011; Khurana et al., 2012; Baumann et
413 al., 2013). The latero-medial gradient of these currents was analyzed in WT and *L9'T*
414 mice.

415 Repeated application of negative voltage steps from -50 to -140 mV, displayed an
416 instantaneous (I_I) followed by a slowly inward (I_s) current (Fig 7A, inset), leading to an I_h

417 (Is- I_l) current. The specificity of this inward current (mediated by HCN channels) was
418 confirmed in all cases by its sensitivity to the selective blocker ZD7288 (Fig 7A, inset).
419 In agreement with previous observations (Leao et al., 2006), I_h currents in WT mice
420 exhibited a medio-lateral gradient (Fig. 7B, -140 mV, M: -372.74±35.48 pA, n=11, 8
421 animals; L: -227.21±32.84 pA, n=7, 6 animals, ANOVA F: 7.89, p=0.013). However, in
422 *L9'T* mice, this difference was absent (M: -381.79±23.95 pA, n=10; 7 animals; L: -
423 332.81±22.27, n=9; 7 animals, ANOVA, F:2.22; p=0.156). The results obtained under
424 voltage-clamp mode were further supported by current-clamp experiments. HCN
425 channels can be activated by a hyperpolarizing current pulse injection which generates
426 a slow "sag" in the membrane potential (Banks et al., 1993; Koch et al., 2004). The sag
427 amplitude in WT medial cells (-51.84±4.13 mV, n=9, 8 animals) was larger compared to
428 that of the lateral region (-39.54±4.78 mV, n=10, 8 animals, ANOVA, F: 5.03; p=0.038).
429 This difference was absent in *L9'T* mice (M: -56.86±6.74 mV, n=7, 6 animals; L: -45±43
430 mV, n=8, 6 animals; ANOVA, F: 2.05; p=0.17).

431 Potassium conductance was elicited in response to 1 s steps from −90 mV to +40 mV
432 in the presence of $CdCl_2$ (50 μM), TTX (3 μM) and ZD7288 (50 μM) to block voltage-
433 dependent calcium, sodium and I_h currents, respectively. Outward currents displayed a
434 fast-small inactivating component and a large delayed non-inactivating component (Fig.
435 7C, inset). Current–voltage relationships displayed topographic differences in WT mice.
436 Thus, at +40 mV the medial MNTB cells exhibited potassium currents of larger
437 amplitude (4.15±0.65 nA, n=6, 5 animals) than those of the lateral cells (2.07±0.11 nA,
438 n=6; 6 animals; Mann-Whitney test, Z:2.72, p=0.0065) (Fig. 7D, inset). In contrast,
439 medio-lateral differences were not observed in *L9'T* mice (M: 4.83±0.99 nA, n=6, 6
440 animals; L: 3.63±0.37 nA, n=7, 6 animals; Mann-Whitney test, Z:1.01, p=0.32). In
441 summary, potassium currents were not topographically distributed in the MNTB of *L9'T*
442 mice.

Discussion

By using mice with a mutation in the α9 nAChR rendering increased suppression of IHC activity (Taranda et al., 2009; Wedemeyer et al., 2018), we show electrophysiological alterations at the glutamatergic MNTB-calyx of Held synapse during the developmental critical period. An overall reduction of MNTB spontaneous spiking activity and synaptic dysfunction together with a lack of latero-medial gradients in several functional properties of the MNTB were observed. These alterations remaining after hearing onset were reflected in the overall ABR wave III amplitude reduction.

It has been suggested that the origin of IHC spontaneous spiking activity is located in the Kölliker's organ that triggers waves of ATP (Tritsch et al., 2007) leading to firing of developing IHCs (Tritsch et al., 2010b; Wang et al., 2015). Alternatively, it has been postulated that spontaneous activity is intrinsically generated by the hair cells (Johnson et al., 2011; 2012). A tight regulation of the pattern of IHC action potentials is a key feature for auditory development (Jonson et al., 2011; 2013; Sendin et al., 2014). Patterned spiking activity is propagated to spiral ganglion cells (Jones et al., 2007; Trisch et al., 2010a; b), brainstem auditory nuclei (Lippe et al., 1995; Sonntag et al., 2009; Trisch et al., 2010a; Clause et al., 2014) and auditory cortex (Babola et al., 2018). Johnson et al. (2011) have suggested that ACh released from efferent terminals is essential for setting a bursting firing pattern in apical IHCs. Moreover, Sendin et al. (2014) have shown that the pharmacological block of α9α10 nAChRs elicits an increase in IHC spontaneous discharge rate. Additionally, normal levels of spontaneous activity in the MNTB, but altered temporal spiking patterns have been reported in α9 knock-out mice (Clause et al., 2014). Since MNTB spontaneous activity is originated in the cochlea (Trisch et al., 2010b), the latter observations most likely arise from the lack of MOC innervation in these mutants and indicate a role of MOC efferent innervation in shaping pre-hearing auditory spontaneous activity. Using a

mouse model with enhanced MOC efferent inhibitory strength, the present results support the notion that the transient α9α10-mediated transmission to IHCs is crucial for modulating spiking-dependent development of the auditory system. Since during development a modest stimulation rate of efferent fibers is sufficient to produce near-maximal inhibition of IHC firing (Moglie et al., 2018), and this inhibition is exacerbated in *L9´T* mutant mice (Wedemeyer et al., 2018), the resultant phenotype most likely results from the silencing of IHC spiking activity. This is supported by the reduction of MNTB multiunit spiking activity observed in the mutants.

Synaptic transmission

In the absence of calcium channels responsible for the release of glutamate by the IHCs, development of synaptic transmission at the calyx of Held is impaired (Erazo-Fischer et al., 2007). Although these mice lack auditory nerve activity, experiments have not clearly distinguished between spontaneous and sound-evoked afferent spiking. The reduction observed in wave III amplitude in the present work can derive from alterations in synaptic transmission at the calyx of Held in *L9'T* mice, since this peak of the ABR is dependent upon synchronous synaptic activity in the MNTB (Melcher et al., 1996; Kim et al., 2013). Thus, the increased number of asynchronic "small"-EPSCs in mutant mice compared to the calyceal-monosynaptic synchronic stimulus intensity-independent EPSCs in WT can account for this phenotypic observation. These asynchronic "small"-EPSCs probably result from a lack of synaptic refinement in *L9´T* mice, a dynamic process that takes place around P2-P4, when calyceal collaterals are pruned, gradually disappear and eventually principal cells end up being contacted by a single calyx of Held (Rodríguez-Contreras et al., 2008; Hoffpauir et al., 2006, 2010; Holcomb et al., 2013). It is interesting to note that although wave III amplitude changes in the mutants were weakest at 8 KHz, synaptic alterations were mainly observed in the lateral low frequency region of the MNTB, an area that

matures significantly later than the medial high frequency region (Ford et al., 2009). This paradoxical result might derive from the fact that wave III reflects auditory processing at the SOC and that this complex comprises several nuclei, including the MNTB (Melcher et al., 1996). Therefore, significant amount of changes and/or compensation mechanisms might take place in other nuclei of the SOC in *L9'T* mice.

The mechanisms leading to the persistence of immature calyces (eliciting asynchronic "small"-EPSCs) in mutant mice is unknown, but most likely reside on the lack of cues needed to strengthen competing synaptic inputs as described for the neuromuscular junction (Wu et al., 2010), the climbing fiber innervation of Purkinje cells (Watanabe and Kano, 2011) and the retinal ganglion cell innervation of the dorsal lateral geniculate nucleus (Hong and Chen, 2011). In this regard, the *L9´T* mutant phenotype resembles that of the bone morphogenetic protein conditional knock-out, with impaired nerve terminal growth, loss of mono-innervation and less mature transmitter release properties (Xiao et al., 2013). It has been reported that developmental pruning of calyceal collaterals is independent of sound-evoked activity (Rodriguez-Contreras et al., 2008). The present results suggest that pruning is dependent upon the transient MOC efferent innervation that tightly controls spontaneous spiking activity.

The increased frequency of mEPSCs in mutant mice might derive from the higher number of cells contacted by multiple calyces. Thus, individual active zones from different axons could independently contribute to spontaneous release. Alternatively, changes in the expression of proteins involved in vesicle docking and priming, as well as Ca^{2+} sensors and other SNARE-binding proteins (Schneggenburger and Rosenmund, 2015), might lead to the same observation. Since evoked synaptic currents were only recorded from principal neurons contacted by a single calyx, the reduction in the amplitude of EPSCs indicates that even in "mono-innervated" synapses, synaptic transmission is altered in *L9´T* mutants. Moreover, the present results show that the intrinsic passive and active properties of MNTB cells, which are

established during the early developmental period (Hoffpauir et al., 2006), were also altered in *L9´T* mutant mice, suggesting upstream alterations in synaptic transmission from the MNTB to lateral SOC, an inhibitory pathway in the mammalian sound localization system (Kandler, 2004).

Tonotopy

Characteristic frequencies of neuronal responses to acoustic stimulation are tonotopically arranged. This is the result of a precise topography of connections that is preserved along the auditory pathway (Friauf and Lohmann, 1999; Rubel and Fritzsch, 2002). This tonotopy is maintained and/or reflected in the topographic arrangement of neuronal functional properties (Li et al., 2001; Barnes-Davies et al. 2004; von Hehn et al. 2004; Brew & Forsythe, 2005; Pienkowski and Harrison, 2005; Leao et al., 2006).

How is tonotopy shaped by spontaneous, sound-independent *versus* sound-evoked auditory nerve activity (Rubel & Fritzsch, 2002; Sanes and Bao, 2009)? Congenitally *dn/dn* deaf mice exhibit alterations in the structural and functional topographic arrangement of several auditory nuclei, indicating disrupted tonotopy (Leao et al., 2006). Although initially considered as a model of disrupted spontaneous spiking activity (Durham et al., 1989), recent findings challenge this hypothesis. Thus, in *dn/dn* mice which bear a deletion in the transmembrane channel-like protein (TMC) 1 (Kurima et al., 2002), prehearing IHCs develop normally and fire spontaneous calcium action potentials (Marcotti et al., 2006).

Experiments performed in α9 knock-out mice have shown normal levels of spontaneous activity in the MNTB but altered temporal spiking patterns (Clause et al., 2014). Moreover, although the overall tonotopy is maintained, the strengthening and silencing of inhibitory MNTB-LSO connections before hearing onset is impaired. This results in a reduced sharpening of functional topography, as the consequence of a

reduction in axonal pruning. In the present work we demonstrate that the enhancement of MOC activity, which leads to an overall reduction in spontaneous MNTB spiking activity, disrupts the topographic specificity of several MNTB characteristics. These include resting membrane potential, action potential waveform and both I_h and potassium currents. Since these conductances allow accurate auditory transmission at high rates across MNTB neurons (Hooper et al., 2002; Barnes-Davies et al., 2004; Hassfurth et al., 2009; Mathews et al., 2010; Karcz et al., 2011; Khurana et al., 2012; Baumann et al., 2013), one could speculate that *L9'T* mice display frequency discrimination impairments, similar to those reported for α9 knock-out mice (Clause et al., 2017). Based on the present results and those of Clause et al. (2014), we propose that the transient MOC efferent innervation to IHCs is a first checkpoint of auditory spontaneous activity. It is interesting to note that the dysfunction of this first checkpoint of IHC activity provided by MOC efferents (as exhibited in α9 knock-out and *L9´T* knock-in mice) is not compensated by homeostatic mechanisms, such as described for *Vglut3* knock-out mice, which lack IHC glutamatergic synaptic transmission (Babola et al., 2018). This might indicate that spontaneous activity in the auditory system is always dictated by the IHCs when these are functionally connected to spiral ganglion neurons. Since central auditory disfunction is observed both in α9 knock-out (Clause et al., 2014) and knock-in mice (present results), the transient MOC efferent transmission to the IHCs most likely provides the patterning and modulation of spiking activity, rather than acting as an on/off switch to spontaneous activity.

References

Bal R, Oertel D (2000) Hyperpolarization-activated, mixed-cation current (I(h)) in octopus cells of the mammalian cochlear nucleus. J Neurophysiol 84:806-817.

Babola TA, Li S, Gribizis A, Lee BJ, Issa JB, Wang HC, Crair MC, Bergles DE (2018) Homeostatic Control of Spontaneous Activity in the Developing Auditory System. Neuron 99:511-524 e515.

Banks MI, Pearce RA, Smith PH (1993) Hyperpolarization-activated cation current (Ih) in neurons of the medial nucleus of the trapezoid body: voltage-clamp analysis and enhancement by norepinephrine and cAMP suggest a modulatory mechanism in the auditory brain stem. J Neurophysiol 70:1420-1432.

Barnes-Davies M, Forsythe ID (1995) Pre- and postsynaptic glutamate receptors at a giant excitatory synapse in rat auditory brainstem slices. J Physiol 488 (Pt 2):387-406.

Barnes-Davies M, Barker MC, Osmani F, Forsythe ID (2004) Kv1 currents mediate a gradient of principal neuron excitability across the tonotopic axis in the rat lateral superior olive. Eur J Neurosci 19:325-333.

Baumann VJ, Lehnert S, Leibold C, Koch U (2013) Tonotopic organization of the hyperpolarization-activated current (Ih) in the mammalian medial superior olive. Front Neural Circuits 7:117.

Boero LE, Castagna VC, Di Guilmi MN, Goutman JD, Elgoyhen AB, Gomez-Casati ME (2018) Enhancement of the Medial Olivocochlear System Prevents Hidden Hearing Loss. J Neurosci 38:7440-7451.

Borst JG, Helmchen F, Sakmann B (1995) Pre- and postsynaptic whole-cell recordings in the medial nucleus of the trapezoid body of the rat. J Physiol 489 (Pt 3):825-840.

Brew HM, Forsythe ID (2005) Systematic variation of potassium current amplitudes across the tonotopic axis of the rat medial nucleus of the trapezoid body. Hear Res 206:116-132.

597 Clause A, Kim G, Sonntag M, Weisz CJ, Vetter DE, Rubsamen R, Kandler K (2014)
598 The precise temporal pattern of prehearing spontaneous activity is necessary for
599 tonotopic map refinement. Neuron 82:822-835.
600 Clause A, Lauer AM, Kandler K (2017) Mice Lacking the Alpha9 Subunit of the
601 Nicotinic Acetylcholine Receptor Exhibit Deficits in Frequency Difference Limens and
602 Sound Localization. Front Cell Neurosci 11:167.
603 Durham D, Rubel EW, Steel KP (1989) Cochlear ablation in deafness mutant mice: 2-
604 deoxyglucose analysis suggests no spontaneous activity of cochlear origin. Hear Res
605 43:39-46.
606 Elgoyhen AB, Johnson DS, Boulter J, Vetter DE, Heinemann S (1994) Alpha 9: an
607 acetylcholine receptor with novel pharmacological properties expressed in rat cochlear
608 hair cells. Cell 79:705-715.
609 Elgoyhen AB, Vetter DE, Katz E, Rothlin CV, Heinemann SF, Boulter J (2001) alpha10:
610 a determinant of nicotinic cholinergic receptor function in mammalian vestibular and
611 cochlear mechanosensory hair cells. Proc Natl Acad Sci U S A 98:3501-3506.
612 Erazo-Fischer E, Striessnig J, Taschenberger H (2007) The role of physiological
613 afferent nerve activity during in vivo maturation of the calyx of Held synapse. J
614 Neurosci 27:1725-1737.
615 Friauf E, Lohmann C (1999) Development of auditory brainstem circuitry. Activity-
616 dependent and activity-independent processes. Cell Tissue Res 297:187-195.
617 Ford MC, Grothe B, Klug A (2009) Fenestration of the calyx of Held occurs sequentially
618 along the tonotopic axis, is influenced by afferent activity, and facilitates glutamate
619 clearance. J Comp Neurol 514:92-106.
620 Gomez-Casati ME, Fuchs PA, Elgoyhen AB, Katz E (2005) Biophysical and
621 pharmacological characterization of nicotinic cholinergic receptors in rat cochlear inner
622 hair cells. J Physiol 566:103-118.
623 Glowatzki E, Fuchs PA (2000) Cholinergic synaptic inhibition of inner hair cells in the
624 neonatal mammalian cochlea. Science 288:2366-2368.

625 Goodman CS, Shatz CJ (1993) Developmental mechanisms that generate precise
626 patterns of neuronal connectivity. Cell 72 Suppl:77-98.
627 Goutman JD, Fuchs PA, Glowatzki E (2005) Facilitating efferent inhibition of inner hair
628 cells in the cochlea of the neonatal rat. J Physiol 566:49-59.
629 Hanson MG, Landmesser LT (2004) Normal patterns of spontaneous activity are
630 required for correct motor axon guidance and the expression of specific guidance
631 molecules. Neuron 43:687-701.
632 Hassfurth B, Magnusson AK, Grothe B, Koch U (2009) Sensory deprivation regulates
633 the development of the hyperpolarization-activated current in auditory brainstem
634 neurons. Eur J Neurosci 30:1227-1238.
635 Hoffpauir BK, Grimes JL, Mathers PH, Spirou GA (2006) Synaptogenesis of the calyx
636 of Held: rapid onset of function and one-to-one morphological innervation. J Neurosci
637 26:5511-5523.
638 Hoffpauir BK, Kolson DR, Mathers PH, Spirou GA (2010) Maturation of synaptic
639 partners: functional phenotype and synaptic organization tuned in synchrony. J Physiol
640 588:4365-4385.
641 Holcomb PS, Hoffpauir BK, Hoyson MC, Jackson DR, Deerinck TJ, Marrs GS, Dehoff
642 M, Wu J, Ellisman MH, Spirou GA (2013) Synaptic inputs compete during rapid
643 formation of the calyx of Held: a new model system for neural development. J Neurosci
644 33:12954-12969.
645 Hong YK, Chen C (2011) Wiring and rewiring of the retinogeniculate synapse. Curr
646 Opin Neurobiol 21:228-237.
647 Hooper SL, Buchman E, Hobbs KH (2002) A computational role for slow conductances:
648 single-neuron models that measure duration. Nat Neurosci 5:552-556.
649 Johnson SL, Eckrich T, Kuhn S, Zampini V, Franz C, Ranatunga KM, Roberts TP,
650 Masetto S, Knipper M, Kros CJ, Marcotti W (2011) Position-dependent patterning of
651 spontaneous action potentials in immature cochlear inner hair cells. Nat Neurosci
652 14:711-717.

653 Johnson SL, Kennedy HJ, Holley MC, Fettiplace R, Marcotti W (2012) The resting
654 transducer current drives spontaneous activity in prehearing mammalian cochlear inner
655 hair cells. J Neurosci 32:10479-10483.
656 Johnson SL, Wedemeyer C, Vetter DE, Adachi R, Holley MC, Elgoyhen AB, Marcotti W
657 (2013) Cholinergic efferent synaptic transmission regulates the maturation of auditory
658 hair cell ribbon synapses. Open Biol 3:130163.
659 Jones TA, Leake PA, Snyder RL, Stakhovskaya O, Bonham B (2007) Spontaneous
660 discharge patterns in cochlear spiral ganglion cells before the onset of hearing in cats.
661 J Neurophysiol 98:1898-1908.
662 Kandler K, Friauf E (1993) Pre- and postnatal development of efferent connections of
663 the cochlear nucleus in the rat. J Comp Neurol 328:161-184.
664 Kandler K (2004) Activity-dependent organization of inhibitory circuits: lessons from the
665 auditory system. Curr Opin Neurobiol 14:96-104.
666 Karcz A, Hennig MH, Robbins CA, Tempel BL, Rubsamen R, Kopp-Scheinpflug C
667 (2011) Low-voltage activated Kv1.1 subunits are crucial for the processing of sound
668 source location in the lateral superior olive in mice. J Physiol 589:1143-1157.
669 Karplus M, Lee C, Cashore WJ, Oh W (1988) The effects of brain bilirubin deposition
670 on auditory brain stem evoked responses in rats. Early Hum Dev 16:185-194.
671 Katz E, Elgoyhen AB, Gomez-Casati ME, Knipper M, Vetter DE, Fuchs PA, Glowatzki
672 E (2004) Developmental regulation of nicotinic synapses on cochlear inner hair cells. J
673 Neurosci 24:7814-7820.
674 Khurana S, Liu Z, Lewis AS, Rosa K, Chetkovich D, Golding NL (2012) An essential
675 role for modulation of hyperpolarization-activated current in the development of
676 binaural temporal precision. J Neurosci 32:2814-2823.
677 Kim SE, Turkington K, Kushmerick C, Kim JH (2013) Central dysmyelination reduces
678 the temporal fidelity of synaptic transmission and the reliability of postsynaptic firing
679 during high-frequency stimulation. J Neurophysiol 110:1621-1630.

680 Kirkby LA, Sack GS, Firl A, Feller MB (2013) A role for correlated spontaneous activity
681 in the assembly of neural circuits. Neuron 80:1129-1144.
682 Koch U, Braun M, Kapfer C, Grothe B (2004) Distribution of HCN1 and HCN2 in rat
683 auditory brainstem nuclei. Eur J Neurosci 20:79-91.
684 Kotak VC, Sanes DH (1995) Synaptically evoked prolonged depolarizations in the
685 developing auditory system. J Neurophysiol 74:1611-1620.
686 Kros CJ, Ruppersberg JP, Rusch A (1998) Expression of a potassium current in inner
687 hair cells during development of hearing in mice. Nature 394:281-284.
688 Kurima K et al. (2002) Dominant and recessive deafness caused by mutations of a
689 novel gene, TMC1, required for cochlear hair-cell function. Nat Genet 30:277-284.
690 Leake PA, Hradek GT, Chair L, Snyder RL (2006) Neonatal deafness results in
691 degraded topographic specificity of auditory nerve projections to the cochlear nucleus
692 in cats. J Comp Neurol 497:13-31.
693 Leao RN, Sun H, Svahn K, Berntson A, Youssoufian M, Paolini AG, Fyffe RE,
694 Walmsley B (2006) Topographic organization in the auditory brainstem of juvenile mice
695 is disrupted in congenital deafness. J Physiol 571:563-578.
696 Li W, Kaczmarek LK, Perney TM (2001) Localization of two high-threshold potassium
697 channel subunits in the rat central auditory system. J Comp Neurol 437:196-218.
698 Lippe WR (1994) Rhythmic spontaneous activity in the developing avian auditory
699 system. J Neurosci 14:1486-1495.
700 Lipovsek M, Im GJ, Franchini LF, Pisciottano F, Katz E, Fuchs PA, Elgoyhen AB (2012)
701 Phylogenetic differences in calcium permeability of the auditory hair cell cholinergic
702 nicotinic receptor. Proc Natl Acad Sci U S A 109:4308-4313.
703 Marcotti W, Johnson SL, Rusch A, Kros CJ (2003) Sodium and calcium currents shape
704 action potentials in immature mouse inner hair cells. J Physiol 552:743-761.
705 Marcotti W, Erven A, Johnson SL, Steel KP, Kros CJ (2006) Tmc1 is necessary for
706 normal functional maturation and survival of inner and outer hair cells in the mouse
707 cochlea. J Physiol 574:677-698.

708 Mathews PJ, Jercog PE, Rinzel J, Scott LL, Golding NL (2010) Control of
709 submillisecond synaptic timing in binaural coincidence detectors by K(v)1 channels.
710 Nat Neurosci 13:601-609.
711 Melcher JR, Knudson IM, Fullerton BC, Guinan JJ, Jr., Norris BE, Kiang NY (1996)
712 Generators of the brainstem auditory evoked potential in cat. I. An experimental
713 approach to their identification. Hear Res 93:1-27.
714 Moglie MJ, Fuchs PA, Elgoyhen AB, Goutman JD (2018) Compartmentalization of
715 antagonistic Ca (2+) signals in developing cochlear hair cells. Proc Natl Acad Sci U S A
716 115:E2095-E2104.
717 Pienkowski M, Harrison RV (2005) Tone frequency maps and receptive fields in the
718 developing chinchilla auditory cortex. J Neurophysiol 93:454-466.
719 Rodriguez-Contreras A, de Lange RP, Lucassen PJ, Borst JG (2006) Branching of
720 calyceal afferents during postnatal development in the rat auditory brainstem. J Comp
721 Neurol 496:214-228.
722 Rodriguez-Contreras A, van Hoeve JS, Habets RL, Locher H, Borst JG (2008)
723 Dynamic development of the calyx of Held synapse. Proc Natl Acad Sci USA
724 105:5603-5608.
725 Rubel EW, Fritzsch B (2002) Auditory system development: primary auditory neurons
726 and their targets. Annu Rev Neurosci 25:51-101.
727 Rusu SI, Borst JG (2010) Developmental changes in intrinsic excitability of principal
728 neurons in the rat medial nucleus of the trapezoid body. Dev Neurobiol 71:284-295.
729 Sanes DH, Bao S (2009) Tuning up the developing auditory CNS. Curr Opin Neurobiol
730 19:188-199.
731 Schneggenburger R, Rosenmund C (2015) Molecular mechanisms governing Ca(2+)
732 regulation of evoked and spontaneous release. Nat Neurosci 18:935-941.
733 Sendin G, Bourien J, Rassendren F, Puel JL, Nouvian R (2014) Spatiotemporal pattern
734 of action potential firing in developing inner hair cells of the mouse cochlea. Proc Natl
735 Acad Sci U S A 111:1999-2004.

736 Shapiro SM (1988) Acute brainstem auditory evoked potential abnormalities in
737 jaundiced Gunn rats given sulfonamide. Pediatr Res 23:306-310.
738 Shaw NA (1988) The auditory evoked potential in the rat--a review. Prog Neurobiol
739 31:19-45.
740 Simmons DD, Mansdorf NB, Kim JH (1996) Olivocochlear innervation of inner and
741 outer hair cells during postnatal maturation: evidence for a waiting period. J Comp
742 Neurol 370:551-562.
743 Sonntag M, Englitz B, Kopp-Scheinpflug C, Rubsamen R (2009) Early postnatal
744 development of spontaneous and acoustically evoked discharge activity of principal
745 cells of the medial nucleus of the trapezoid body: an in vivo study in mice. J Neurosci
746 29:9510-9520.
747 Taranda J, Maison SF, Ballestero JA, Katz E, Savino J, Vetter DE, Boulter J, Liberman
748 MC, Fuchs PA, Elgoyhen AB (2009) A point mutation in the hair cell nicotinic
749 cholinergic receptor prolongs cochlear inhibition and enhances noise protection. PLoS
750 Biol 7:e18.
751 Taschenberger H, Leao RM, Rowland KC, Spirou GA, von Gersdorff H (2002)
752 Optimizing synaptic architecture and efficiency for high-frequency transmission. Neuron
753 36:1127-1143.
754 Taschenberger H, Scheuss V, Neher E (2005) Release kinetics, quantal parameters
755 and their modulation during short-term depression at a developing synapse in the rat
756 CNS. J Physiol 568:513-537.
757 Tritsch NX, Yi E, Gale JE, Glowatzki E, Bergles DE (2007) The origin of spontaneous
758 activity in the developing auditory system. Nature 450:50-55.
759 Tritsch NX, Rodriguez-Contreras A, Crins TT, Wang HC, Borst JG, Bergles DE (2010a)
760 Calcium action potentials in hair cells pattern auditory neuron activity before hearing
761 onset. Nat Neurosci 13:1050-1052.
762 Tritsch NX, Bergles DE (2010b) Developmental regulation of spontaneous activity in
763 the Mammalian cochlea. J Neurosci 30:1539-1550.

764 Vetter DE, Liberman MC, Mann J, Barhanin J, Boulter J, Brown MC, Saffiote-Kolman J,
765 Heinemann SF, Elgoyhen AB (1999) Role of alpha9 nicotinic ACh receptor subunits in
766 the development and function of cochlear efferent innervation. Neuron 23:93-103.
767 Vetter DE, Katz E, Maison SF, Taranda J, Turcan S, Ballestero J, Liberman MC,
768 Elgoyhen AB, Boulter J (2007) The alpha10 nicotinic acetylcholine receptor subunit is
769 required for normal synaptic function and integrity of the olivocochlear system. Proc
770 Natl Acad Sci U S A 104:20594-20599.
771 von Hehn CA, Bhattacharjee A, Kaczmarek LK (2004) Loss of Kv3.1 tonotopicity and
772 alterations in cAMP response element-binding protein signaling in central auditory
773 neurons of hearing impaired mice. J Neurosci 24:1936-1940.
774 Wang HC, Lin CC, Cheung R, Zhang-Hooks Y, Agarwal A, Ellis-Davies G, Rock J,
775 Bergles DE (2015) Spontaneous Activity of Cochlear Hair Cells Triggered by Fluid
776 Secretion Mechanism in Adjacent Support Cells. Cell 163:1348-1359.
777 Warr WB, Guinan JJ, Jr. (1979) Efferent innervation of the organ of corti: two separate
778 systems. Brain Res 173:152-155.
779 Watanabe M, Kano M (2011) Climbing fiber synapse elimination in cerebellar Purkinje
780 cells. Eur J Neurosci 34:1697-1710.
781 Wedemeyer C, Vattino LG, Moglie MJ, Ballestero J, Maison SF, Di Guilmi MN, Taranda
782 J, Liberman MC, Fuchs PA, Katz E, Elgoyhen AB (2018) A Gain-of-Function Mutation
783 in the alpha9 Nicotinic Acetylcholine Receptor Alters Medial Olivocochlear Efferent
784 Short-Term Synaptic Plasticity. J Neurosci 38:3939-3954.
785 Weisstaub N, Vetter DE, Elgoyhen AB, Katz E (2002) The alpha9alpha10 nicotinic
786 acetylcholine receptor is permeable to and is modulated by divalent cations. Hear Res
787 167:122-135.
788 Wimmer VC, Horstmann H, Groh A, Kuner T (2006) Donut-like topology of synaptic
789 vesicles with a central cluster of mitochondria wrapped into membrane protrusions: a
790 novel structure-function module of the adult calyx of Held. J Neurosci 26:109-116.

791 Wu H, Xiong WC, Mei L (2010) To build a synapse: signaling pathways in
792 neuromuscular junction assembly. Development 137:1017-1033.
793 Xiao L, Michalski N, Kronander E, Gjoni E, Genoud C, Knott G, Schneggenburger R
794 (2013) BMP signaling specifies the development of a large and fast CNS synapse. Nat
795 Neurosci 16:856-864.
796 Yi E, Roux I, Glowatzki E (2010) Dendritic HCN channels shape excitatory postsynaptic
797 potentials at the inner hair cell afferent synapse in the mammalian cochlea. J
798 Neurophysiol 103:2532-2543.
799

800 **Figure Legends**

801 **Figure 1. The overall MNTB activity is lower in *L9'T* mice**

802 **A**. Representative recordings acquired with a polytrode from WT (black) and *L9'T* (red)
803 mice. **B**. Quantification of the averaged multi-unit activity per animal. Box plot
804 displaying the larger average of multi-unit activity in WT (11.49±3.58 Hz, n=6 animals)
805 compared to *L9'T* mice (2.53-±0.43 Hz, n=8 animals; Mann-Whitney U Test, Z=2.19,
806 p=0.028). Boxes represent interquartile range between 25-75%, whiskers indicate the
807 minimum and maximum of all data and the inside square is the median.

808

809 **Figure 2. Auditory brainstem response of wave III was smaller in *L9'T*** mice **at**
810 **P21.**

811 **A**. Schematic diagram of the brainstem at the level of the superior olivary complex
812 showing the cochlear stimulation with a speaker. Representative traces of auditory
813 brainstem responses (ABR) of WT (black) and *L9'T* (red) mice at 80 dB SPL/32 kHz
814 showing waves I, II and III (bottom) at P21. ABR wave I (**B**), wave II (**C**) and wave III
815 (**D**) amplitudes at 80 dB SPL for 8, 16 and 32 kHz at P16 and P21. At P21, no
816 significant differences were found for waves I and II at any of the frequencies tested. At
817 this developmental age, however, *L9'T* mice had lower wave III amplitudes at all the
818 frequencies tested (ANOVA, $p<0.05$). Bars represent the mean ± SEM. See also Table
819 1.

820

821 **Figure 3. Altered Spontaneous Synaptic Transmission in *L9'T* mice.**

822 **A.** Representative traces of miniature excitatory postsynaptic currents (mEPSCs) for
823 WT M (black), WT L (grey), *L9'T* M (red) and *L9'T* L (pink) inP12-P14 mice. Examples
824 of two different cells are shown for both genotypes. **B. i.** mEPSCs amplitude

histograms displaying a similar data distribution for WT and *L9'T*. **B. ii.** The mean mEPSCs amplitude for all conditions displayed no significant differences (WT M: n=8 cells/7 animals, WT L: n=12 cells/8 animals, ANOVA, F: 1.21; p=0.285; *L9'T* M: n=18 cells/14 animals, *L9'T* L: n=16 cells/13 animals, Mann-Whitney test, Z: -0.66, p=0.512). **C. i**. Data distribution for mEPSC frequency comparing WT and *L9'T* genotypes. The fitting with a Gaussian function evidenced that higher frequencies were more represented in *L9'T* mice. **C. ii.** mEPSCs frequency was similar for medial and lateral cells in WT mice (ANOVA, F:1.16, p=0.689). However, it was increased in the lateral region of *L9'T* mice (Mann-Whitney test, Z: -2.11; p=0.035).

Figure 4. Altered Evoked-Synaptic Transmission in *L9'T* mice.

Representative traces of evoked excitatory post synaptic currents (EPSCs) of MNTB principal cells for WT (black) and *L9'T* (red) at P12-14 (**A**) and P20-24 (**E**)**.** Histogram distribution of EPSC amplitudes for both genotypes at different developmental stages (**B** and **F**). Note that in these cases, histogram fitting with a Gaussian curve evidenced larger tails at lower amplitudes in *L9'T* mice. **C.** Averaged traces of EPSCs for WT M (black), WT L (grey), *L9'T* M (red) and *L9'T* L (pink). **D.** At P12-14 the mean EPSC amplitude was similar along the tonotopic map in WT (M: n=9 cells/7 animals, L: n=10 cells/8 animals, ANOVA, F: 0.027, p=0.87) but not in *L9'T* mice where the mean EPSC amplitude decreased in the lateral side (M: n=11cells/11 animals, L: n=12 cells/11 animals, ANOVA, F: 5.07, p=0.0357). **G**. Average traces at P20-24 for WT M (black), WT L (grey), *L9'T* M (red) and *L9'T* L (pink). **H**. The mean EPSC amplitude was similar for both WT (M: n=5 cells/5 animals, L: n=5 cells/4 animals, ANOVA, F:0.0242, p=0.881) and *L9'T* (M: n=6 cells/6 animals; L: n=9 cells/5 animals; F:0.05246, p=0.82) mice. Note that in all cases, evoked synaptic currents were only recorded from principal neurons displaying EPSCS independent of stimulus intensity. The lack of statistical

significance is most likely due to the larger data dispersion in the mutant mice (CV_{WT}: 0.241; $CV_{L9'T}$: 0.681). Bars represent the mean ± SEM.

Figure 5. Small-EPSCs were observed more frequently in *L9'T* mice.

A. Representative traces of two types of EPSCs evoked in MNTB principal neurons by stimulation of the trapezoid body. A large EPSC coming from a calyceal terminal (left) and small-EPCSs from multiple terminals (right). Arrows indicate the position of the stimulation artifact. Cell-attached recordings (loose-patch configuration, upper traces) show action potential currents on MNTB cells. EPSCs were recorded in the whole cell configuration (lower traces). Note that calyceal EPSCs did not increase whereas small-EPSCs amplitude increased with higher stimulus intensity. (Inset) Input–output curve shows a graded increase in EPSC amplitude with increasing stimulation intensity for "small"-EPSCs but an all-or-none behavior for "large"-EPSCs (mean ± SEM). **B.** Percentage of cells with small or large inputs. A larger proportion of small amplitude connections was observed in *L9'T* mice. In WT mice small-EPSCs were 10% (4 of 35 cells, 11 animals), whereas this proportion was three-fold larger in *L9'T* mice (31%; 12 of 38 cells / 12 animals; Chi-squared test, χ^2=4.32, df=1, p=0.019).

Figure 6. AP shape differed along the tonotopic axis in WT but not in *L9'T* mice.

A. Upper: Superimposed action Potential (AP) waveform of WT (black) and *L9'T* (red) MNTB cells. Filled lines represent the medial and dashed lines the lateral side. Bottom: APs were aligned to their absolute amplitude showing that they reach similar peak voltages. **B**. The resting membrane potential (RMP) was more depolarized for medial than lateral cells in WT mice (M: n=7 cells/5 animals; L: n=6 cells/5 animals, ANOVA, F: 9.33, p=0.0013). However, no medio-lateral differences were detected in *L9'T* (M: n=8 cells/7 animals; L: n=7 cells/7 animals, ANOVA, F: 0.136, p=0.72). AP features

were quantified: AP amplitude (**C**), After hyperpolarization (AHP; **D**), area (**E**) and AP delay (**F**). Note that in all cases, mediolateral differences in WT AP waveform were abolished in *L9'T* mice. Bars represent the mean ± SEM. See additional information on Table 2.

Figure 7. Medio-lateral gradient of potassium currents was absent in *L9'T* mice.

A. I-V relationship for I_h currents exhibited a medio-lateral gradient in WT, but this topographic difference disappeared in *L9'T* mice. Bars represent the mean ± SEM. **Inset**. Representative traces of I_h currents (WT medial) elicited by hyperpolarizing voltage steps from -50 to -140 mV every 10 s for 0.5 s (right). Current responses consisted of an instantaneous inward current (I_I) and a slowly developing inward current (I_S). I_h amplitudes were determined as I_S-I_I. Representative I_h trace at -140 mV after bath perfusion with the specific HCN channel blocker ZD 7288 (50 µM, left). **B**. Quantification of maximal I_h current amplitude at -140 mV for WT (M: n=11 cells/8 animals; L: n=7 cells/6 animals, ANOVA, F: 7.89, p=0.013) and *L9'T* mice (M: n=10 cells/7 animals; L: n=9 cells/7 animals, ANOVA, F: 2.22; p=0.156). **C**. I-V relationship displayed a larger potassium current in medial compared to lateral cells in WT mice whereas this tonotopic distribution was absent in *L9'T* mice (bars represent the mean ± SEM). **Inset**. Representative traces at different depolarizing voltage steps (from -90 to +40mV; 5 mV increment during 1s) in the presence of TTX (3 µM), $CdCl_2$ (50 µM) and ZD7288 (50 µM). Potassium currents were measured in the steady-state region (within the last 50 ms, green dashed lines). **D.** Maximal K^+ current amplitude at +40 mV exhibits a medio-lateral gradient for WT (M: n=6 cells/5 animals; L: n=6 cells/6 animals; Mann-Whitney test, Z: 2.72, p=0.0065) but not in *L9'T* mice (M: n=6 cells/6 animals; L: n=7 cells/6 animals, Mann-Whitney test, Z: 1.01, p=0.32).

Table 1. ABR peak amplitudes quantification at P16 and P21

904

905 **Table 2. ABR latencies quantification at P16 and P21**

906

907 **Table 3. Action potential features**

Figure 1 - JN-RM-2536-18-R2

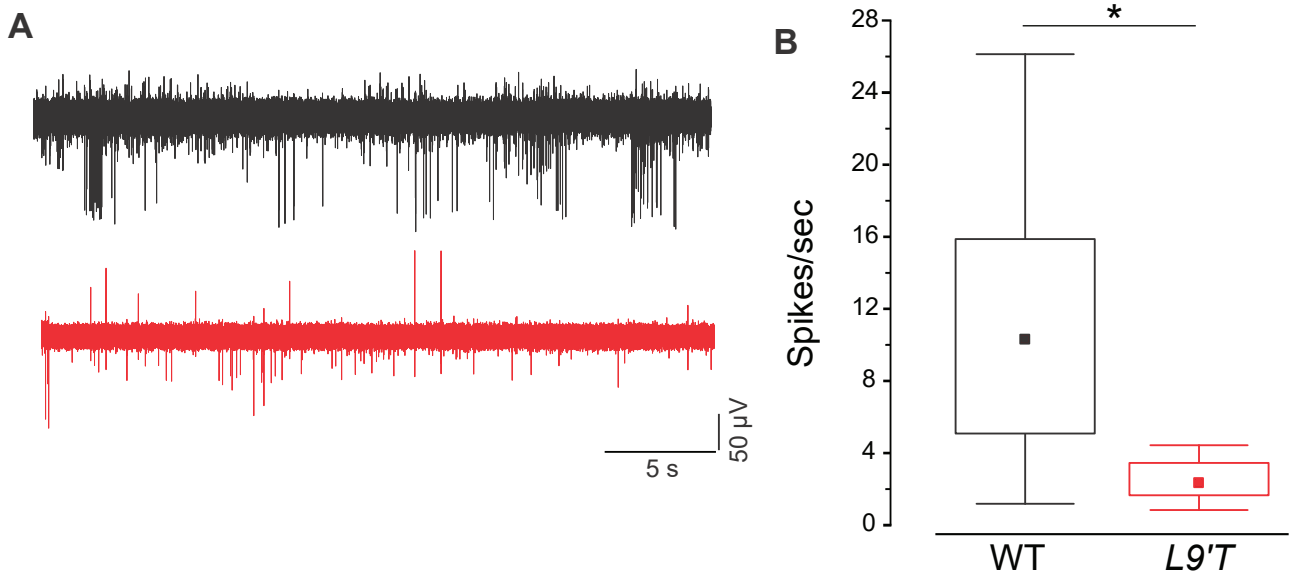

Figure 2- JN-RM-2536-18-R2

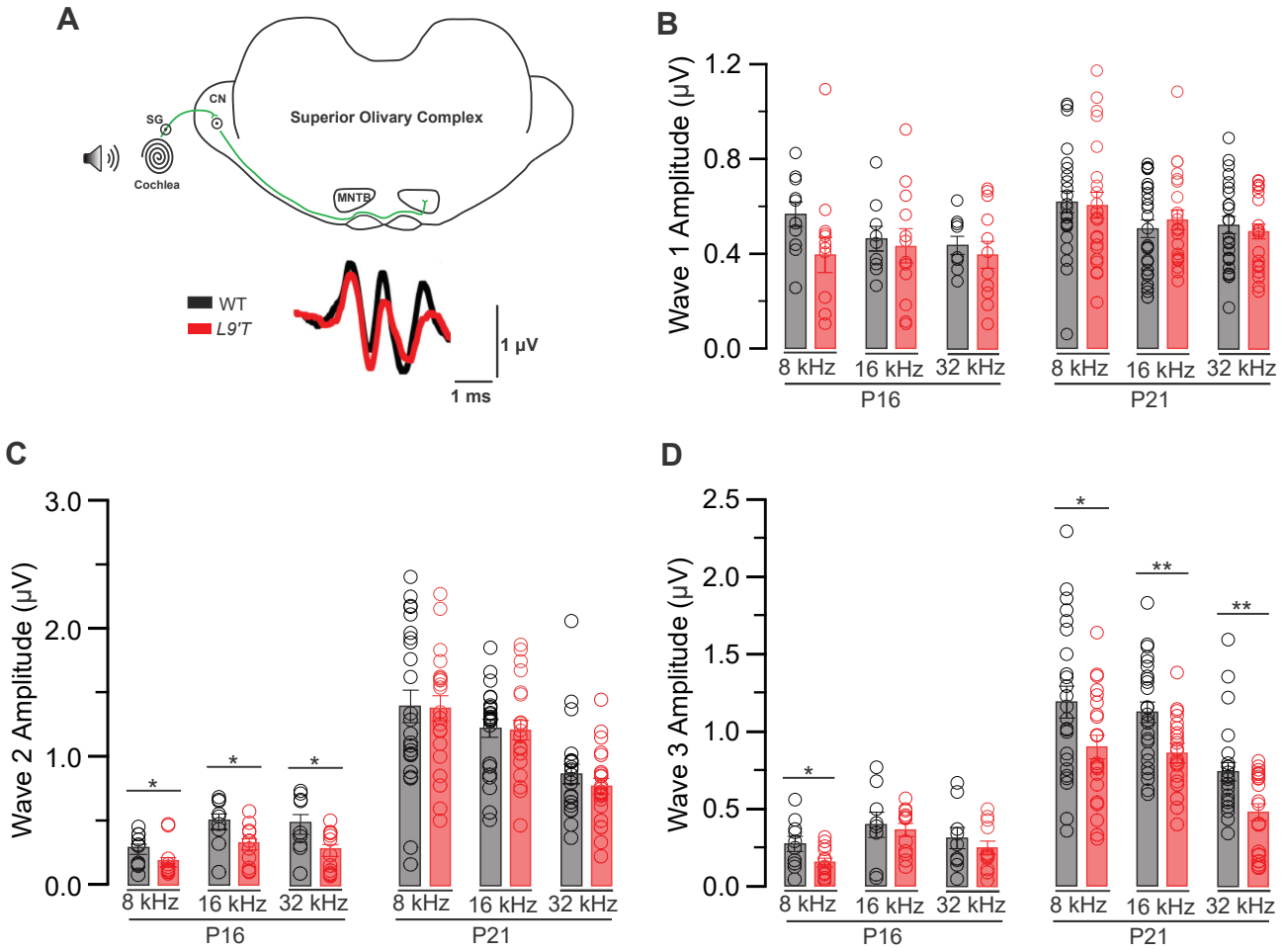

Figure 3 - JN-RM-2536-18-R2

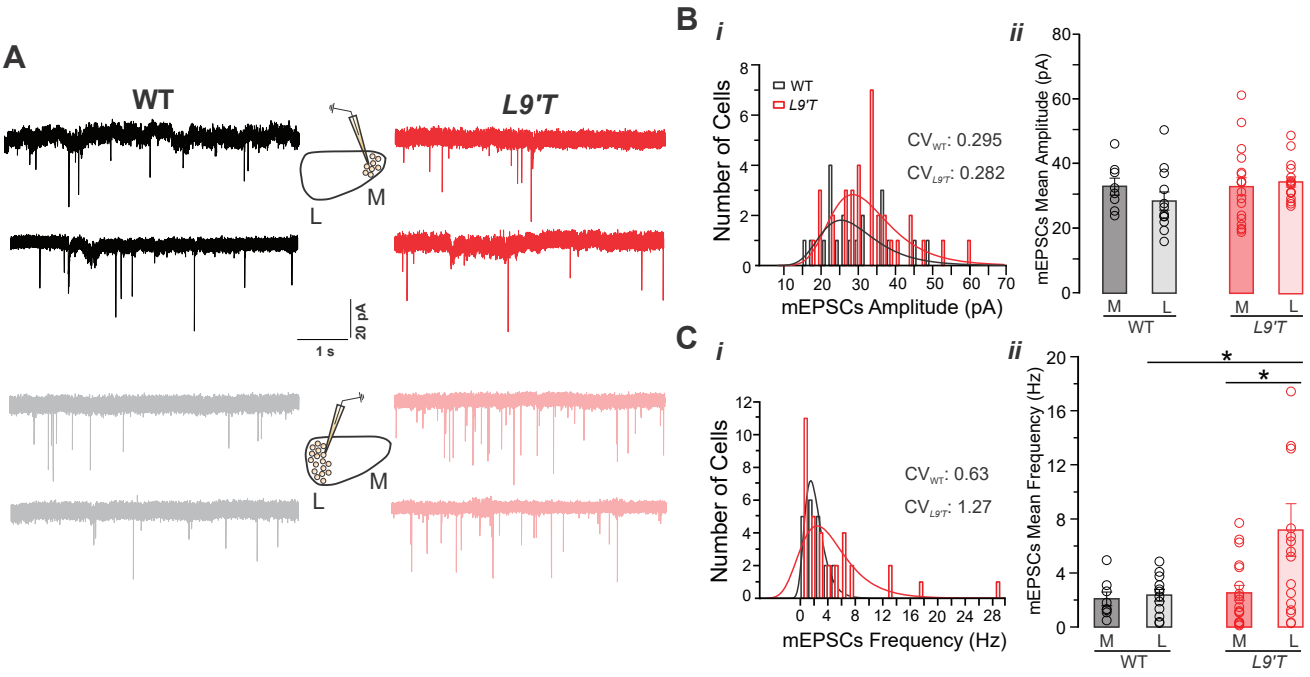

Figure 4 - JN-RM-2536-18-R2

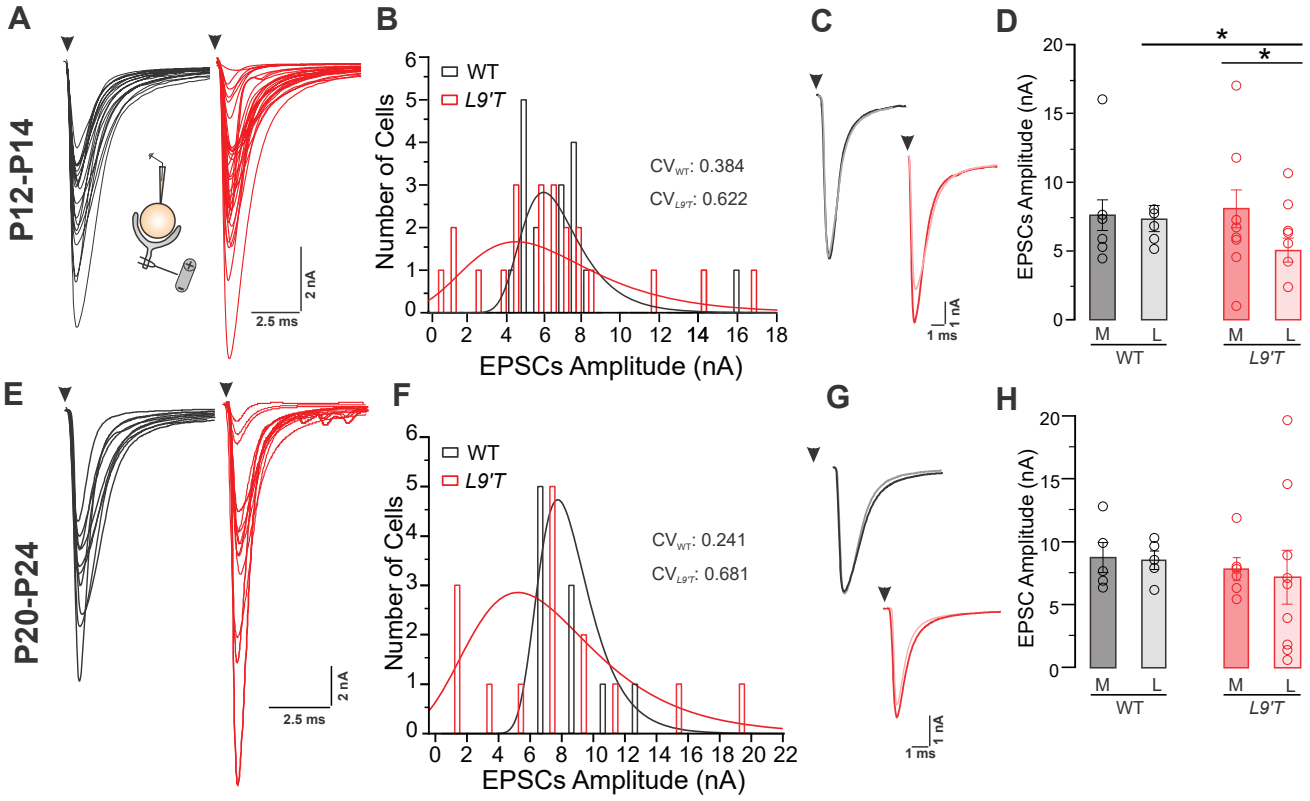

Figure 5 - JN-RM-2536-18-R2

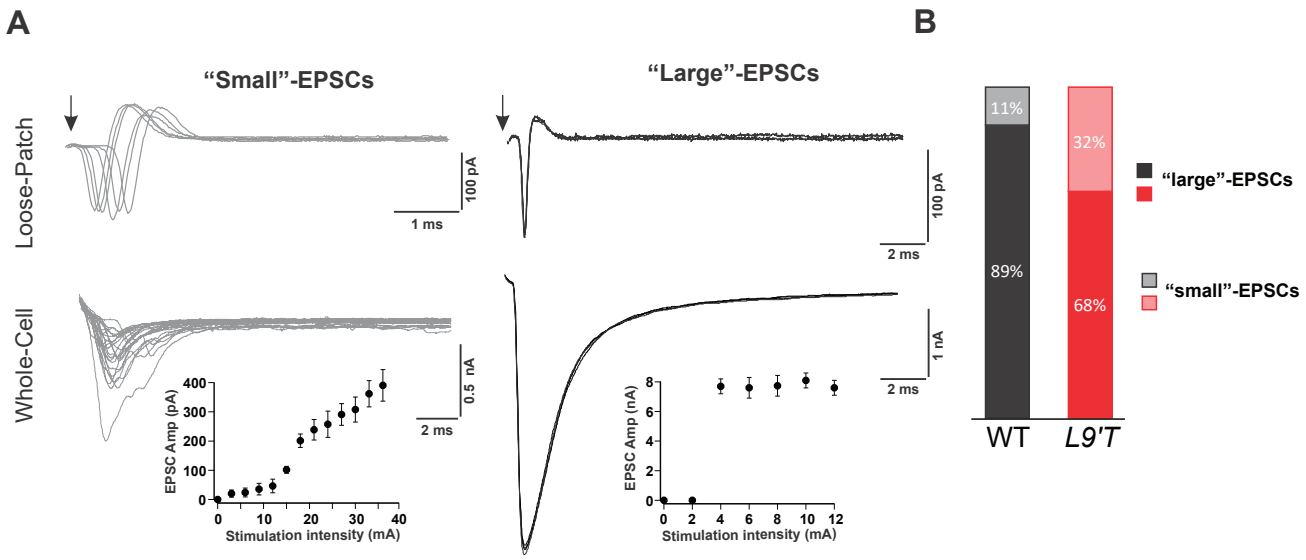

Figure 6 - JN-RM-2536-18-R2

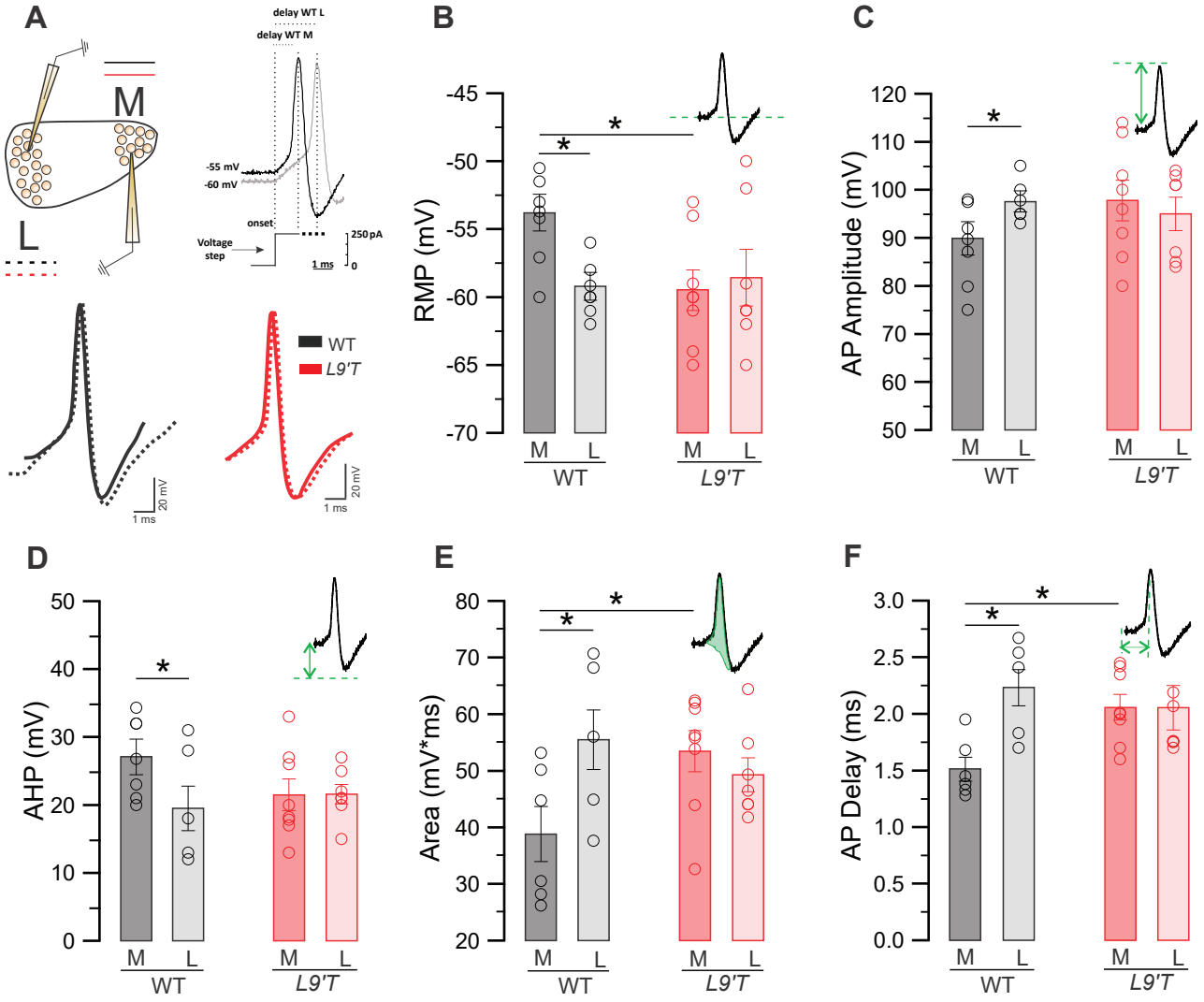

Figure 7 - JN-RM-2536-18-R2

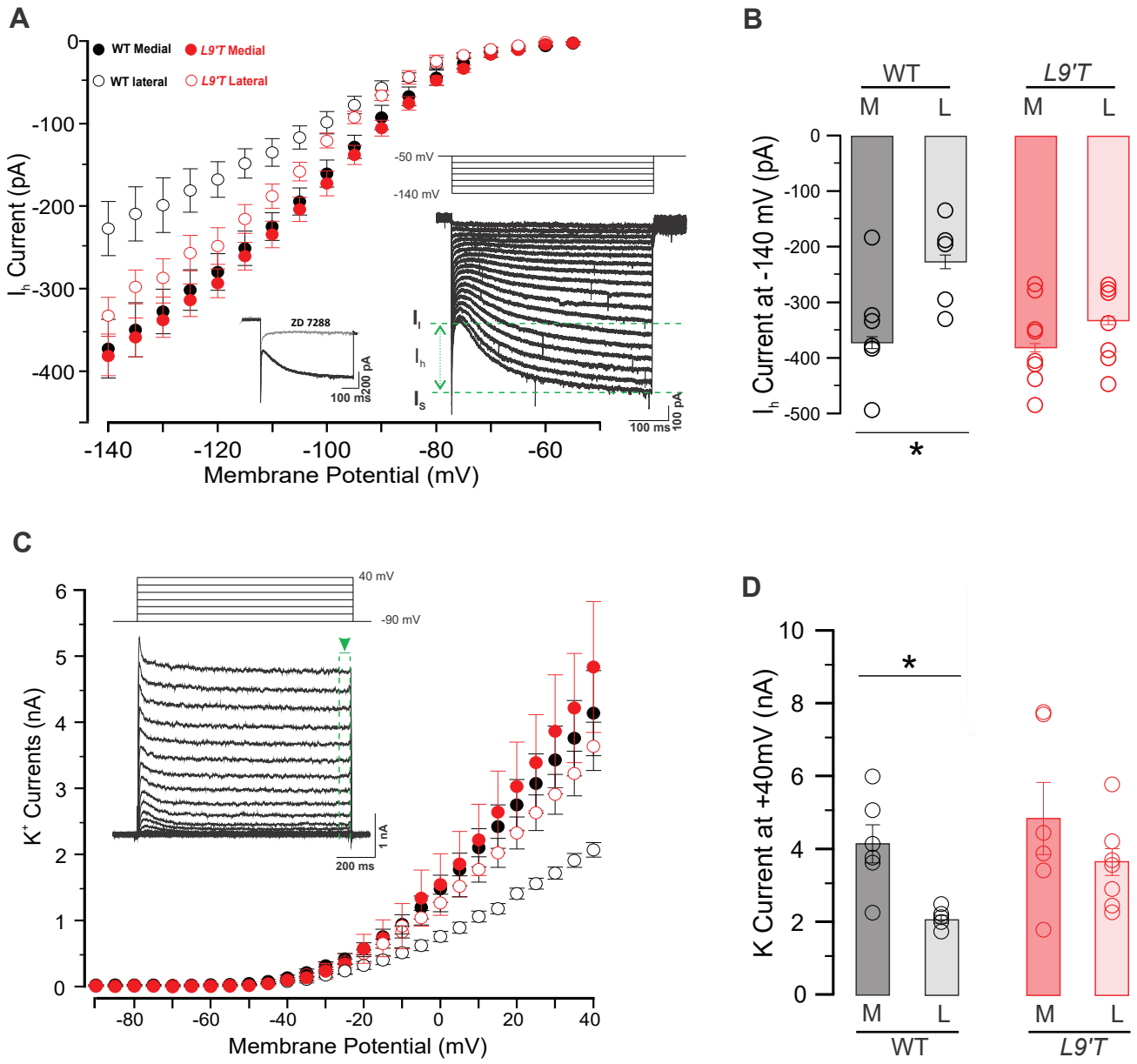

Table 1 - JN-RM-2536-18

		Peak I		Peak II		Peak III		Peak IV		Peak V		ratio PIII/PI		n	
		WT	*L9'T*	WT	*L9'T*	WT	*L9'T*	WT	*L9'T*	WT	*L9'T*	WT	*L9'T*	WT	*L9'T*
P16	**8 KHz**	0.57±0.05	0.39±0.08	0.28±0.04	0.17±0.04 [1]	0.28±0.05	0.16±0.03 [4]	0.36±0.04	0.24±0.03 [5]	0.46±0.04	0.29±0.03 [7]	0.53±0.11	0.71±0.19	10	13
	16 KHz	0.47±0.05	0.44±0.07	0.48±0.06	0.31±0.04 [2]	0.39±0.08	0.36±0.04	0.37±0.06	0.34±0.04	0.28±0.03	0.24±0.03	0.92±0.23	1.13±0.24	9	12
	32 KHz	0.44±0.04	0.44±0.06	0.47±0.07	0.26±0.05 [3]	0.31±0.07	0.25±0.04	0.41±0.06	0.25±0.04 [6]	0.31±0.02	0.24±0.02 [8]	0.82±0.24	0.83±0.21	9	12
P21	**8 KHz**	0.62±0.05	0.61±0.06	1.39±0.13	1.37±0.09	1.19±0.10	0.90±0.08 [9]	0.37±0.06	0.27±0.04	0.33±0.05	0.26±0.04	2.18±0.25	1.81±0.25	24	22
	16 KHz	0.51±0.04	0.55±0.04	1.22±0.07	1.21±0.08	1.13±0.07	0.86±0.05 [10]	0.51±0.09	0.26±0.04	0.35±0.05	0.36±0.05	2.55±0.25	1.77±0.16 [12]	25	22
	32 KHz	0.52±0.04	0.50±0.03	0.86±0.08	0.76±0.06	0.74±0.06	0.48±0.06 [11]	0.29±0.05	0.32±0.04	0.25±0.04	0.31±0.04	1.49±0.09	1.03±0.14 [13]	24	22

[1]F:3.55, p=0.05; [2]F:5.78, p=0.027; [3]F:6.07, p=0.023; [4]F:5.10, p=0.035; [5]F: 6.22, p=0.021; [6]F: 4.89, p=0.038; [7]F: 11.39; p=0.0028; [8]F: 4.16, p=0.05; [9]F:5.02, p=0.031;

[10]F:9.7, p=0.0032; [11]F:10.22, p=0.0026; [12]F: 5.69, p=0.0021; [13]F: 7.43, p=0.0092

Table 2 - JN-RM-2536-18

		Latency to Peak I		Latency to Peak II		Latency to Peak III		Latency to Peak IV		Latency to Peak V		n	
		WT	*L9'T*	WT	*L9'T*	WT	*L9'T*	WT	*L9'T*	WT	*L9'T*	WT	*L9'T*
P16	**8 KHz**	1.41±0.08	1.61±0.05	2.29±0.09	2.31±0.05	3.39±0.15	3.61±0.11	4.48±0.18	4.37±0.06	5.41±0.25	5.77±0.09	10	13
	16 KHz	1.46±0.06	1.61±0.06	2.36±0.09	2.34±0.05	3.78±0.14	3.63±0.12	4.65±0.35	4.73±0.05	6.06±0.17	5.72±0.09	9	12
	32 KHz	1.33±0.05	1.39±0.04	2.31±0.06	2.41±0.03	3.42±0.15	3.58±0.06	4.38±0.14	4.71±0.11	5.44±0.23	5.58±0.11	9	12
P21	**8 KHz**	1.69±0.02	1.79±0.04	2.47±0.06	2.32±0.11	3.83±0.07	4.17±0.16	4.79±0.12	4.33±0.19	6.07±0.18	5.76±0.23	24	22
	16 KHz	1.69±0.03	1.73±0.04	2.45±0.06	2.42±0.09	3.97±0.08	4.23±0.15	4.95±0.09	4.73±0.19	6.05±0.14	5.96±0.23	25	22
	32 KHz	1.36±0.02	1.41±0.04	2.28±0.03	2.38±0.07	3.59±0.06	3.51±0.14	4.51±0.11	4.18±0.15	5.82±0.15	5.38±0.21	24	22

Table 3 - JN-RM-2536-18

	WT		*L9'T*	
	M	**L**	**M**	**L**
Amplitude (mV)	89.88±1.41 (n=7)	97.61±0.98 (n=6)[1]	97.75±1.49 (n=8)	95.01±1.31 (n=7)
AHP (mV)	27.05±1.07 (n=7)	19.50±1.54 (n=8)[2]	21.5±0.82 (n=8)	21.57±0.54 (n=7)
Area (mV*ms)	38.83±1.99 (n=6)	55.49±2.14 (n=6)[3]	53.48±1.29 (n=8)	49.29±1.14 (n=7)
Delay (ms)	1.51±0.04 (n=6)	2.23±0.07 (n=6)[4]	2.06±0.04 (n=8)	2.05±0.07 (n=7)

[1]F: 5.518, p=0.038; [2]F: 4.678, p=0.045; [3]F: 5.418, p=0.042; [4]F: 14.185, p=0.0037